

# PhaRaO: Direct Radar Odometry using Phase Correlation

Yeong Sang Park<sup>1</sup>, Young-Sik Shin<sup>2</sup> and Ayoung Kim<sup>1\*</sup>

**Abstract**—Recent studies in radar-based navigation present promising navigation performance using scanning radars. These scanning radar-based odometry methods are mostly feature-based; they detect and match salient features within a radar image. Differing from existing feature-based methods, this paper reports on a method using *direct* radar odometry, PhaRaO, which infers relative motion from a pair of radar scans via phase correlation. Specifically, we apply the Fourier Mellin transform (FMT) for Cartesian and log-polar radar images to sequentially estimate rotation and translation. In doing so, we decouple rotation and translation estimations in a coarse-to-fine manner to achieve real-time performance. The proposed method is evaluated using large-scale radar data obtained from various environments. The inferred trajectory yields a 2.34% (translation) and 2.93° (rotation) Relative Error (RE) over a 4 km path length on average for the odometry estimation.

## I. INTRODUCTION

The development of robot perception in recent decades has increased the potential for robot navigation in extreme environments. Most widely utilized perceptual sensors include Light Detection and Ranging (LiDAR) and cameras; however, these sensors may limit a robot's sensing due to short-range perception. Radar, however, shows a longer range measurement and is robust to environmental variances, such as light and in-air particles.

Recent studies show promising performance using the radar for odometry estimation within a larger-scale environment. These reported radar odometry methods mostly exploit feature-based methods by using an adaptive threshold method called constant false alarm rate (CFAR) to extract radar features. Automotive radars leverage this CFAR feature, but the resulting features may be very sparse and inconsistent [1]. Unlike automotive radars, scanning radars provide relatively high angular and range resolution, encouraging further radar odometry studies. For example, Cen and Newman [2] proposed a new feature extraction and data association method via graph matching [2, 3]. Aldera et al. [4] performed pre-filtering using weak supervision [4]. These aforementioned feature-based approaches could be meaningful because the radar's range is very large and less likely to experience a feature-less region. Still, these approaches could be limited because they focus on a portion of the entire scene, thus losing an overall context.

Unlike feature-based approaches, direct methods focus on the entire image by examining the correlation of two sequential radar images in the Fourier domain. Some researchers

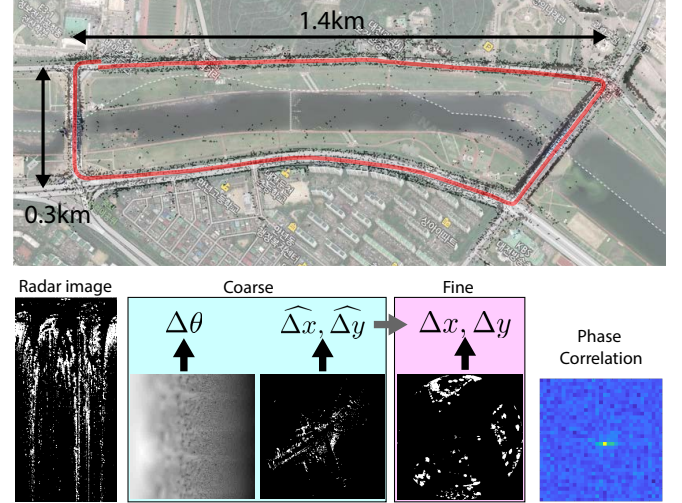


Fig. 1. Overview of the proposed method and resulting estimated trajectory. The bottom row shows sample images used in the coarse-to-fine FMT. On the top, the estimated trajectory (red) is overlaid over the aerial image together with back-projected radar points based on the odometry estimation.

presented these direct approaches using phase correlation and kernel cross-correlation [5, 6]. Direct methods are less likely to fall into local minima than feature-based methods, even in the featureless environment because they calculate the full image's correlation. Exploiting this characteristic, one strategy was introduced by using this phase correlation as the initial value for a 2D LiDAR Iterated Closest Point (ICP) [7]. For underwater, Hurtós et al. [8] exploited the FMT over imaging sonar for promising performance in underwater simultaneous localization and mapping (SLAM) and reconstruction. For radar sensors, Checchin et al. [9] proposed SLAM using FMT and extended Kalman filter (EKF). Vivet et al. created clean radar images using a sensing-distortion analysis for FMT to increase accuracy [10, 11].

Despite this meaningful performance over noisy images, these direct methods come with a high computational cost. The long range radar accumulates a large amount of information from each ray. The Fourier domain calculation involves a high computational load when applying the direct approaches. This paper presents a direct real-time radar odometry (RO), PhaRaO, that overcomes this main challenge by leveraging phase correlation between two radar image frames. The proposed two-phase method presents accuracy and computational efficiency in the odometry. The proposed method's attributes are:

- We decouple the rotation and translational estimations in the proposed coarse-to-fine approach, as shown in Fig. 1. We generate a coarse image by down-sampling

<sup>1</sup> Y. Park and A. Kim are with the Department of Civil and Environmental Engineering, KAIST, Daejeon, S. Korea. [pys0728k, ayoungk]@kaist.ac.kr

<sup>2</sup> Y. Shin is with Korea Institute of Machinery and Materials, Daejeon, S. Korea. yshin86@kimm.re.kr

only in the radial direction. Due to the up-sampling effect when converting from down-sampled Cartesian to log-polar, the estimated rotation from this coarse log-polar image estimates the accurate rotation component that we use for the translational estimation.

- By applying this coarse-to-fine two-phase estimation, the overall computational cost is substantially reduced, which allows for real-time support of 10 Hz on average.

## II. METHOD

As illustrated in Fig. 2, the proposed direct radar odometry method consists of four parts: (i) the pre-processing module, (ii) a phase correlation to estimate the relative translation and heading between radar images, (iii) the odometry selection module and (iv) a local graph optimization to refine the estimated poses. Each module is described in the following subsections.

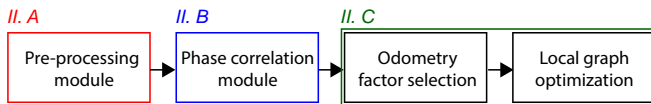


Fig. 2. A flowchart of entire system including four modules. Each upperletter means corresponding subsection.

### A. Radar Image Pre-processing

Phase correlation is commonly used in image processing when computing a transformation from the linear shift between two images. Another widely exploited pre-processing method for this transformation inference is to convert an image into a log-polar image and apply phase correlation, thereby obtaining a relative rotation from a linear shift. Because raw radar measurements are provided as polar images, directly applying phase correlation to the full-size raw images seems plausible. Unfortunately, however, the angular resolution is too low even in the full resolution to accurately estimate the relative rotation. As a solution to this issue, we applied FMT to the log-polar image computed from the down-sampled Cartesian image. Due to the high-pass filter, fast Fourier transform (FFT), and interpolation during

the Cartesian and the log-polar conversion, the resulting log-polar image allows for a more accurate angular resolution, yielding an up-sampling effect in the angular direction. We refer to [12] for more detail.

We also considered applying phase correlation to full-size Cartesian images for translation estimation and to log-polar images for rotation estimation. However, when performing FFT over converted Cartesian images, the computational cost of the increased resolution becomes unrealistic (e.g., the size of Cartesian radar image used in this paper is  $6720 \times 6720$ ). Furthermore, we found that raw radar images are quite noisy, so there could be a risk of falling into the local minima when the direct method is applied.

Therefore, prior to computing the phase correlation, we prepared three pre-calculated images, as shown in Fig. 3. Given a raw radar image, we resized the raw radar image in a down-sample radial direction and a coarse polar image then converted this to a coarse Cartesian and log-polar image. Together with these coarse images, a Cartesian image in the original resolution was prepared for the refinement phase. Each frame  $\mathbf{F}_t$  consists of three images as  $\mathbf{F}_t = \{D_c, D_p, F_c\}$ , whereas each image indicates a down-sampled Cartesian image  $D_c$ , a down-sampled log-polar image  $D_p$  and a full-resolution Cartesian sub-image  $F_c$ , respectively.

### B. Phase Correlation

Using the three images generated during radar image pre-processing, we computed phase correlation to infer the relative motion between the frames by applying FMT as in [9]. Under translation shift  $\Delta x, \Delta y$ , relation between the current image  $I_t(x, y)$  and the previous image  $I_{t-n}(x, y)$  can be written as

$$I_t(x, y) = I_{t-n}(x - \Delta x, y - \Delta y). \quad (1)$$

Applying FFT on both sides modifies the equation as

$$\begin{aligned} \hat{I}_t(u, v) &= \mathcal{F}(I_t(x, y)) \\ &= \hat{I}_{t-n}(u, v) \cdot e^{-i(u\Delta x + v\Delta y)}. \end{aligned} \quad (2)$$

From the normalized cross power spectrum defined as,

$$\begin{aligned} \hat{P}(u, v) &= \frac{\hat{I}_t \hat{I}_{t-n}^*}{|\hat{I}_t \hat{I}_{t-n}^*|} = e^{-i(u\Delta x + v\Delta y)} \\ P(x, y) &= \mathcal{F}^{-1}(\hat{P}(u, v)), \end{aligned} \quad (3)$$

the relative translation  $\Delta x, \Delta y$  is calculated by solving the following equation.

$$\Delta x, \Delta y = \operatorname{argmax}_{x, y} \{P(x, y)\}. \quad (4)$$

FMT performs phase correlation by converting the Cartesian image to a log-polar image. Thus, the scale and rotation difference can be calculated as a translation term. We leveraged phase correlation at two levels as follows (see also Fig. 4).

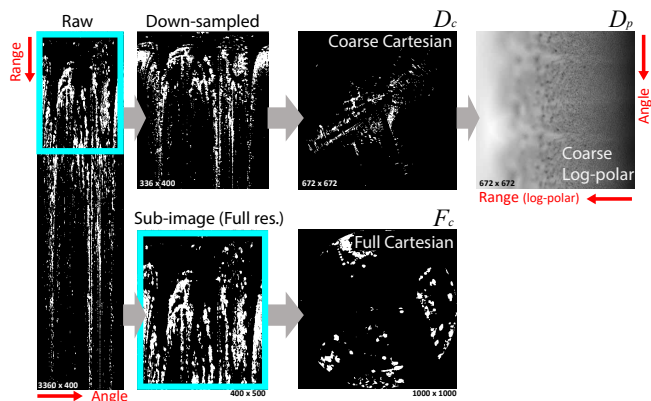


Fig. 3. Image preparation for dual-phase radar image registration. Given a raw image, we compute three types of pre-computed images  $D_c$ ,  $D_p$ , and  $F_c$ . Cyan box indicates the region where the ROI for sub-image is set.

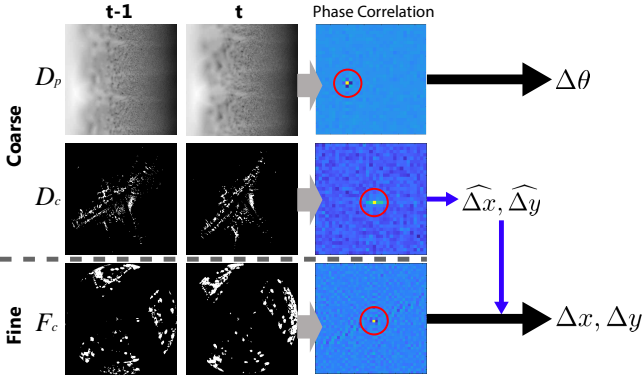


Fig. 4. Details of odometry calculation using phase correlation. Each pre-computed images produces a different component of the odometry. Given a two sequential frames between  $t - 1$  and  $t$ , we compute each component from phase correlation. The red circle indicates the estimated motion component via phase correlation.

1) *Transformation from a down-sampled image*: The proposed method estimates initial  $\widehat{\Delta x}$ ,  $\widehat{\Delta y}$ , and  $\Delta\theta$  by performing FMT with the down-sampled image. Because the image used here is down-sampled only in the radial direction,  $\Delta\theta$  preserves the full resolution. Phase correlation at the coarse image level eliminates noise and highlights context, allowing for robust estimation. By performing phase correlation on the down-sampled log-polar image, we computed the initial estimation of rotation ( $\Delta\theta$ ). We then applied this rotation to adjust the down-sampled Cartesian image to compute  $\widehat{\Delta x}$  and  $\widehat{\Delta y}$ .

2) *Refine translation from Cartesian sub-image*: By exploiting a sub-image of the raw image center, we refined the translational estimation and substantially improved computation speed. Still, challenges remain, such as noise-induced local minima and less rotation distinguishability from small ROI. To minimize these disadvantages, we estimated rotation from coarse images and only refined translations within the surrounding grid.

### C. Local Graph Optimization

Low angular resolution and high noise level may encumber successful phase correlation between consecutive images if

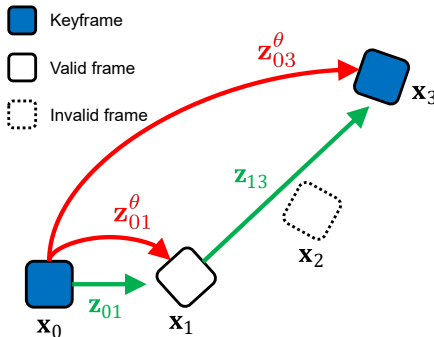


Fig. 5. Selected nodes are depicted in a solid lined box and keyframes appear in blue boxes. Red lines indicate heading factor between keyframes and green lines shows valid odometry factors. If a radar image associated with a node is less informative (e.g.,  $x_2$ ), odometry factor is recomputed by skipping the meaningless node.

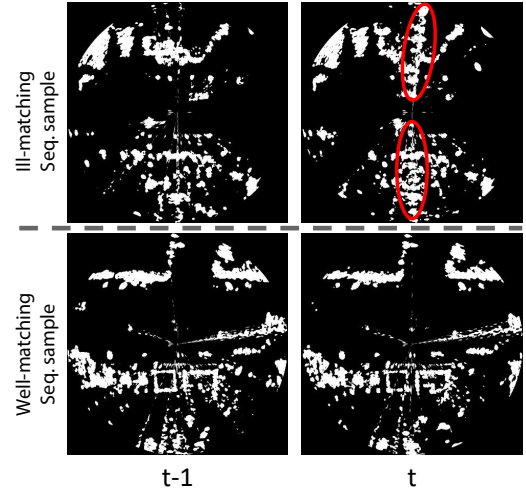


Fig. 6. Two representative Cartesian images from less-informative and informative radar image pair. Red circles in the ill-matching pair sample indicate the ghost return from multipath. The informative node selection prune out node associated with less informative images thereby achieving reliable estimation.

the incoming image is less informative. To alleviate this issue and improve odometry estimation, we ran a local graph optimization with odometry and keyframe selection. This procedure is described in Fig. 5. By checking consistency criteria, we only selected plausible odometry and informative keyframes. These sorted keyframes were further utilized as heading correction factors.

1) *Informative Node Selection*: We performed odometry factor and keyframe selection as shown in Fig. 5. The proposed algorithm aimed at finding an image pair that yields reliable motion estimation. We needed criteria for filtering inaccurate values out. The following confidence levels were chosen for consistency criteria.

$$C_f(\mathbf{z}_{(i,j)}) = \exp\left(-\left|\tan^{-1} \frac{\Delta y_{i,j}}{\Delta x_{i,j}} - \Delta\theta_{i,j}\right|\right) \quad (5)$$

The confidence level is high when the discrepancy between the translational ( $\Delta x, \Delta y$ ) and rotational ( $\Delta\theta$ ) components is small. Only when  $C_f(\mathbf{z}_{(t-1,t)}) > \alpha$ , the pose node and pose factor  $\mathbf{z}_{(t-1,t)}$  are included in the graph. Sample images in Fig. 6 shows exemplary images on how this module performs for informative node selection.

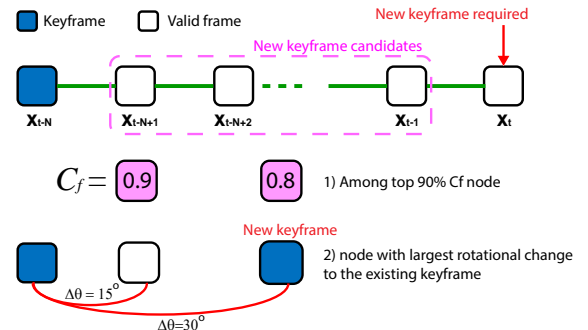


Fig. 7. When a new keyframe is required, we select the new keyframe using confidence level and rotation against the previous keyframe.

2) *Keyframe Selection*: The odometry factor is continuously added to the graph until a new keyframe is determined. When the new keyframe is determined, all nodes are dropped from the sliding window and the graph starts again at the new keyframe. The new keyframe is added when

- The graph's total numbers exceed the maximum sliding window size  $W$ . In this paper,  $W = 5$  is used.
- The cost of the initial keyframe ( $\mathbf{x}_{t-N,t-1}$ ) compared to the current frame ( $\mathbf{x}_t$ ) is less than the cost compared to the previous frame ( $\mathbf{x}_{t-1}$ ). When this happens, the correlation of subsequent images becomes worse, and a new keyframe is needed.  $C_f(\mathbf{z}_{(t-N,t-1)}) > C_f(\mathbf{z}_{(t-N,t)})$
- The accumulated distance from the initial keyframe exceeds the maximum range. The traversed distance exceeds the radar's range, and a new keyframe is required.

When the abovementioned cases occur, we add a new keyframe. The keyframe is selected from the local window, as shown in Fig. 7. We first define a feasible set  $\mathcal{K}$  by only considering the top 90% of the valid frames within the window using the confidence level  $C_f$ .

$$\mathcal{K} = \{i \mid C_f(\mathbf{z}_{(t-N,i)}) > \beta \cdot \max \mathbf{C}_f, \beta = 0.9\} \quad (6)$$

The new keyframe then becomes the node with the largest rotational motion compared to the previous keyframe.

$$\operatorname{argmax}_{i \in \mathcal{K}} \Delta\theta_{t-N,i} \quad (7)$$

3) *Local Pose Graph Definition*: We created a local pose graph using 2D pose  $\mathbf{x} = (\mathbf{x}_{t-N}, \dots, \mathbf{x}_t)^T$ . In this local pose graph, two types of internode factors were used. First, a carefully selected odometry factor between meaningful frames was added to the local graph to connect the nodes. In addition to these odometry constraints, we added heading correction factors associated with keyframes that were robust to the rotational estimation. Using these two types of constraints, we solved for the graph optimization problem using incremental smoothing and mapping (iSAM) [13] as

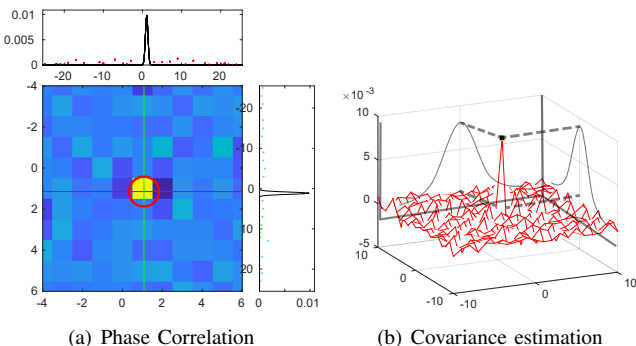


Fig. 8. Uncertainty modeling illustration. Given the phase correlation results in (a), we fit Gaussian distribution to estimate the covariance for the radar odometry constraint.

below.

$$\begin{aligned} e_{ij}(\mathbf{x}_i, \mathbf{x}_j) &= \mathbf{z}_{ij} - \hat{\mathbf{z}}_{ij}(\mathbf{x}_i, \mathbf{x}_j) \\ \mathbf{F}(\mathbf{x}) &= \sum_{\langle i,j \rangle \in C} e_{ij}^T \Omega_{ij} e_{ij} \\ \mathbf{x}^* &= \operatorname{argmin}_{\mathbf{x}} \{\mathbf{F}(\mathbf{x})\} \end{aligned} \quad (8)$$

Here, measurement  $\mathbf{z}$  implies both an odometry factor and a heading factor.

4) *Uncertainty Estimation*: When solving pose-graph SLAM in the local window, the covariance estimation for each constraint is critical. For radar odometry uncertainty modeling, we similarly followed the method introduced in [8]. This method regards the amplitude values around the main peak of the cross power spectrum as localization inaccuracies. These values are fitted to the Gaussian ellipse to obtain translation and rotation uncertainties ( $\sigma_x, \sigma_y, \sigma_\theta$ ) as shown in Fig. 8. Since these values are pixel values, they are converted to metric values using range resolution  $\delta_r$  (pixels/m) and  $\delta_\theta$  (pixels/rad). In this paper, the confidence level  $C_f$  proposed in factor selection is also used to weight uncertainty modeling.

$$\Omega^{\mathbf{z}} = C_f \cdot \begin{bmatrix} (\sigma_x \delta_r)^2 & 0 & 0 \\ 0 & (\sigma_y \delta_r)^2 & 0 \\ 0 & 0 & (\sigma_\theta \delta_\theta)^2 \end{bmatrix}^{-1}. \quad (9)$$

Lastly, the heading correction factor uncertainty is as given below:

$$\Omega^{\mathbf{z}^\theta} = k \cdot C_f \cdot [(\sigma_\theta \delta_\theta)^2]^{-1}. \quad (10)$$

The same confidence level was used, but it was multiplied by a constant  $k > 1$  to rely more on the heading correction factor. Specifically,  $k = 10$  was empirically selected and weight more on heading correction between keyframes.

### III. EXPERIMENTAL RESULTS

We evaluated the proposed radar odometry using a publicly available radar datasets [14, 15]. Target environments can be seen from aerial and radar image samples in Fig. 9. In the evaluation phase, we examined the effects of the detailed module together with the computational cost analysis. Both qualitative and quantitative evaluations are presented.

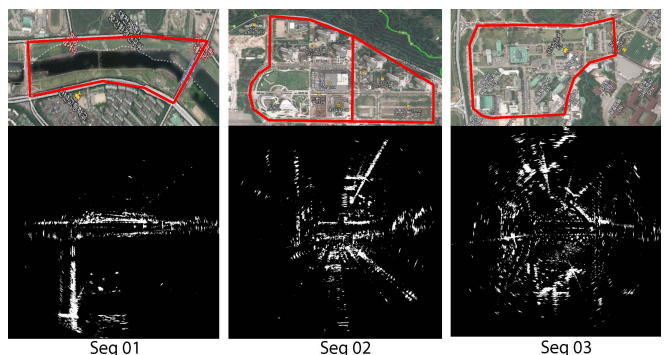


Fig. 9. Aerial image and sample radar images from each sequence.

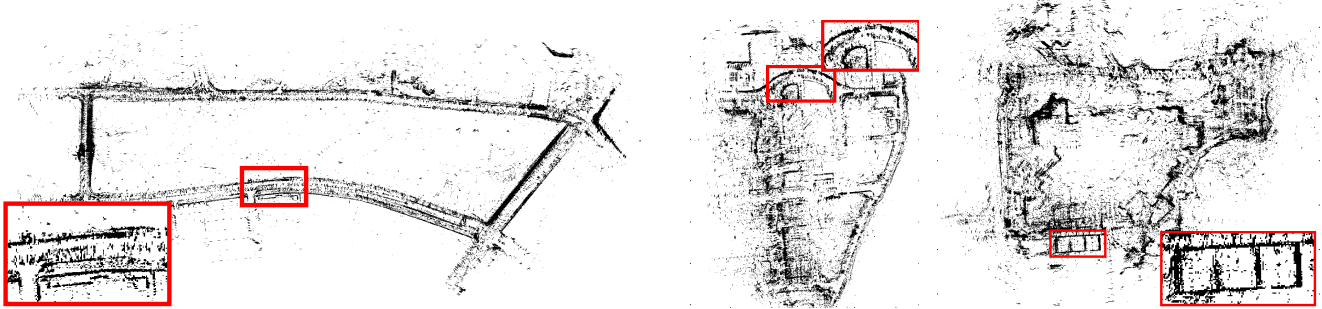


Fig. 10. Radar map generated using estimated odometry. Black dots represent back-projected radar points using estimated odometry. The proposed method has been evaluated over three different environments from [14, 15] with structural and scale variation. Zoomed views are illustrated in red boxes.

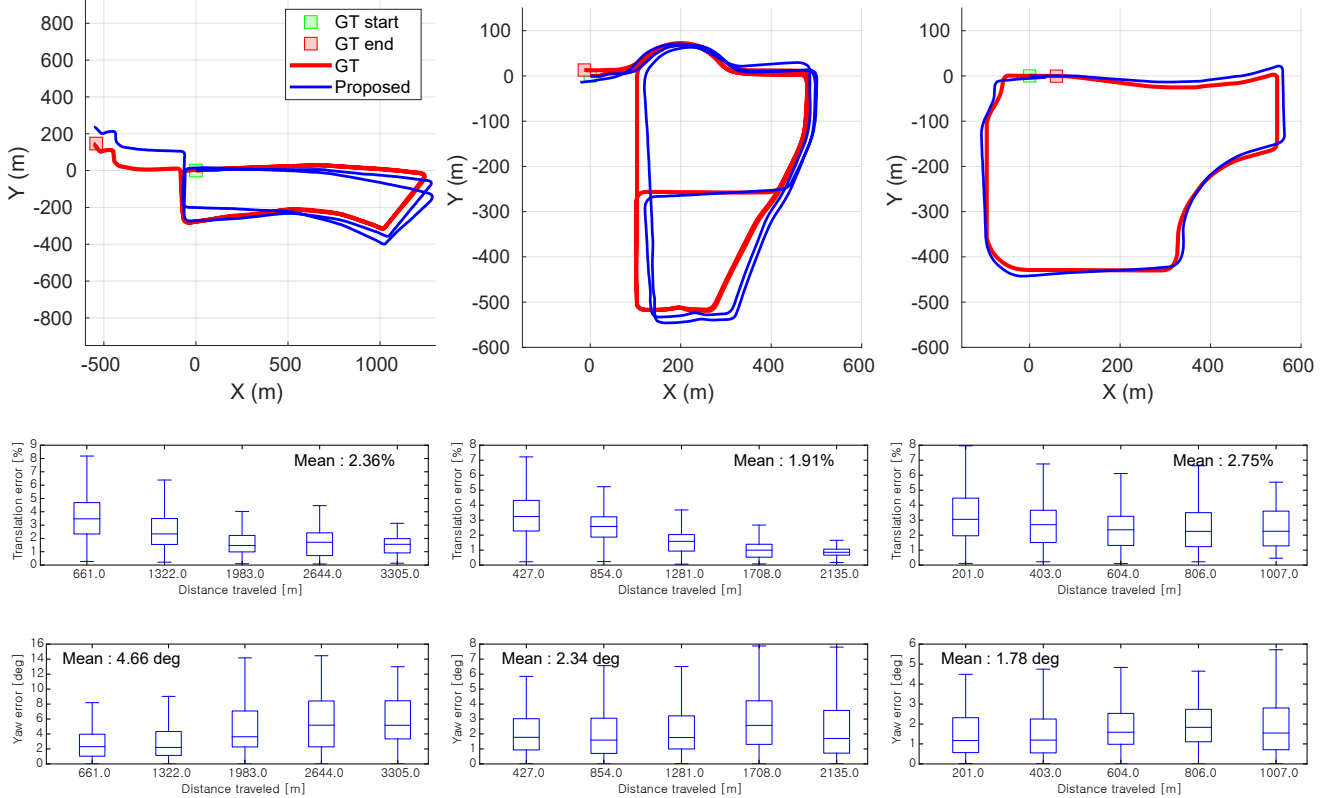


Fig. 11. Evaluation of the proposed method; trajectories (first row), percentage of relative translation errors with a mean value (second row), and relative heading errors with a mean value (third row). Each column means the evaluation with diffent type of sequences.

TABLE I

ABSOLUTE TRAJECTORY ERROR (RMSE)

Seq No.	Path len. [m]	Full Module		Local Graph Opt. (Only Coarse Img.)		Coarse to Fine Reg.		Only Coarse Reg.	
		Trans. [m]	Rot. [deg]	Trans. [m]	Rot. [deg]	Trans. [m]	Rot. [deg]	Trans. [m]	Rot. [deg]
1	6612.6	31.83	0.077	53.37	0.085	87.48	0.180	83.93	0.179
2	4273.4	12.08	0.041	56.56	0.138	136.93	0.489	132.78	0.480
3	2018.5	13.26	0.029	20.47	0.059	67.16	0.242	69.59	0.252

### A. Dataset and Evaluation Metric

**Dataset:** The proposed radar odometry was evaluated over three different sequences from [14, 15]. These sequences include various structural diversity levels. The sample radar images are shown in Fig. 9. All sequences included radar

measurement and ground truth trajectory. The datasets provided radar images captured using a Navtech CIR204-H scanning radar, which has  $360^\circ$  per 400 samples, a maximum range of 200 m, 3360 range bins, and a range resolution of approximately 0.06 m, operating in 4 Hz.

**Evaluation metric:** For evaluation, we compared the estimated trajectory against the provided ground truth trajectory. The performance of the radar odometry was evaluated in terms of absolute trajectory error (ATE) and RE using the evaluation procedure presented in [16].

### B. Odometry Evaluation

The overall estimated trajectories are depicted in Fig. 11. All three sequences are large scale ranging from 2 km to 6 km. The first and second sequences had multiple repeated routes. The estimated trajectory captured the overall trajectory even after a long traverse distance. The bottom row of Fig. 11 shows the RE of the trajectory, translation, and rotation. The trajectory is aligned with the start position of the ground truth following [16]. The average translation RE were low and well maintained from 1.91 to 2.75%. For all sequences, the rotational RE showed a promising performance over kilometers of path length. As additional qualitative evaluation, we back-projected the radar images using the estimated odometry, as shown in Fig. 10.

As ablation studies, we examined the effect of each module on overall radar odometry performance in terms of the ATE. Table I shows ATE for each module of the method. As listed in the table, naive coarse-to-fine image registration may perform worse than coarse image registration. Because fine images may have poor image context that causes FMT to fail or produce incorrect values. However, after filtering the low correlation images through factor selection, the local module optimization results in a performance that is 4.7 times faster and 3.4 times better than estimations based only on coarse images. Furthermore, when the local graph optimization module is included, it results in a significant improvement compared to the other case. Finally, keyframe selection shows that the partial heading correction constraints have a significant effect.

### C. Computational Cost

The computational time for each module is depicted in a stacked area plot in Fig. 12. The overall algorithm runs at

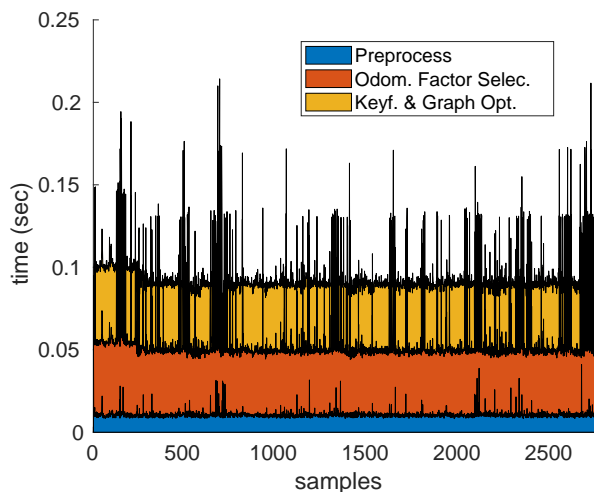


Fig. 12. Area plot of each module’s computation time. The total time still is under 0.1 sec on average allowing 10 Hz of real-time performance.

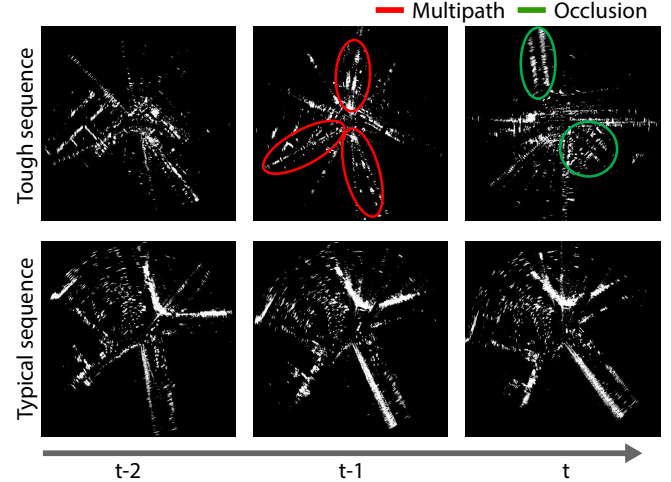


Fig. 13. Sample sequence when the radar odometry could be misleading (tough sequence) in comparison to a typical sequence. The three images in each row are three consecutive radar images. On the top sudden multipath induced returns created ghost effects (red circles) at  $t - 1$ . Even more challenging example abruptly appears at  $t$  when hidden structures from previous frames appears as in the green circles.

10.73 Hz on average. The pre-processing 11.6%, odometry factor selection 46.9%, and keyframe selection and graph optimization 41.5% still enable real-time performance. The most computationally demanding modules are odometry factor selection and keyframe selection because of the phase correction computation. The proposed algorithm was evaluated on a desktop PC with an i7-7700K CPU and 32 GB of RAM without using the GPU.

### D. Challenges in Radar Odometry

Although radar is robust to weather conditions perceiving at longer range, we encountered several challenging cases during odometry estimation. A challenging example is depicted together with another typical sequence sample in Fig. 13. The multipath return is a well-known artifact in the radar images. We also found that occlusion sometimes occurs, revealing hidden structures from the previous frames. However, since the proposed method relies on both coarse and fine level cues for odometry estimation, the estimated odometry was able to robustly estimate the motion in spite of these challenges.

## IV. CONCLUSION

This paper reported a *direct* radar-based odometry estimation methods that uses phase correlation. By introducing the odometry factor between nodes and heading correction factor between keyframes, the algorithm achieved less than 3% RE over three sets of sequences. The multi-resolution approach enabled real-time performance. The algorithm runs at 10 Hz on average, fully facilitating real-time operation. In the future, we plan to examine image pre-processing for full-resolution sub-images and further improve overall performance.

## REFERENCES

- [1] M. Rapp, M. Barjenbruch, M. Hahn, J. Dickmann, and K. Dietmayer, “Probabilistic ego-motion estimation using multiple automotive radar sensors,” *Robotics and Autonomous Systems*, vol. 89, pp. 136–146, 2017.
- [2] S. H. Cen and P. Newman, “Radar-only ego-motion estimation in difficult settings via graph matching,” *arXiv preprint arXiv:1904.11476*, 2019.
- [3] ——, “Precise ego-motion estimation with millimeter-wave radar under diverse and challenging conditions,” in *2018 IEEE International Conference on Robotics and Automation (ICRA)*. IEEE, 2018, pp. 1–8.
- [4] R. Aldera, D. De Martini, M. Gadd, and P. Newman, “Fast radar motion estimation with a learnt focus of attention using weak supervision,” in *Proceedings of the IEEE International Conference on Robotics and Automation (ICRA), Montreal, Canada*, 2019.
- [5] C. Wang, L. Zhang, L. Xie, and J. Yuan, “Kernel cross-correlator,” in *Thirty-Second AAAI Conference on Artificial Intelligence*, 2018.
- [6] C. Wang, T. Ji, T.-M. Nguyen, and L. Xie, “Correlation flow: robust optical flow using kernel cross-correlators,” in *2018 IEEE International Conference on Robotics and Automation (ICRA)*. IEEE, 2018, pp. 836–841.
- [7] G. Jiang, L. Yin, G. Liu, W. Xi, and Y. Ou, “Fft-based scan-matching for slam applications with low-cost laser range finders,” *Applied Sciences*, vol. 9, no. 1, p. 41, 2019.
- [8] N. Hurtós, D. Ribas, X. Cuffí, Y. Petillot, and J. Salvi, “Fourier-based registration for robust forward-looking sonar mosaicing in low-visibility underwater environments,” *Journal of Field Robotics*, vol. 32, no. 1, pp. 123–151, 2015.
- [9] P. Checchin, F. Gérossier, C. Blanc, R. Chapuis, and L. Trassoudaine, “Radar scan matching slam using the fourier-mellin transform,” in *Field and Service Robotics*. Springer, 2010, pp. 151–161.
- [10] D. Vivet, F. Gérossier, P. Checchin, L. Trassoudaine, and R. Chapuis, “Mobile ground-based radar sensor for localization and mapping: An evaluation of two approaches,” *International Journal of Advanced Robotic Systems*, vol. 10, no. 8, p. 307, 2013.
- [11] D. Vivet, P. Checchin, and R. Chapuis, “Radar-only localization and mapping for ground vehicle at high speed and for riverside boat,” in *2012 IEEE International Conference on Robotics and Automation*. IEEE, 2012, pp. 2618–2624.
- [12] B. S. Reddy and B. N. Chatterji, “An fft-based technique for translation, rotation, and scale-invariant image registration,” *IEEE transactions on image processing*, vol. 5, no. 8, pp. 1266–1271, 1996.
- [13] M. Kaess, A. Ranganathan, and F. Dellaert, “isam: Incremental smoothing and mapping,” *IEEE Transactions on Robotics*, vol. 24, no. 6, pp. 1365–1378, 2008.
- [14] G. Kim, Y. S. Park, Y. Cho, J. Jeong, and A. Kim, “Mulran: Multimodal range dataset for urban place recognition,” in *IEEE International Conference on Robotics and Automation (ICRA)*, 2020, accepted. To appear.
- [15] Y. S. Park, J. Jeong, Y. Shin, and A. Kim, “Radar dataset for robust localization and mapping in urban environment,” in *ICRA Workshop on Dataset Generation and Benchmarking of SLAM Algorithms for Robotics and VR/AR*, Montreal, May. 2019.
- [16] Z. Zhang and D. Scaramuzza, “A tutorial on quantitative trajectory evaluation for visual (-inertial) odometry,” in *2018 IEEE/RSJ International Conference on Intelligent Robots and Systems (IROS)*. IEEE, 2018, pp. 7244–7251.